ChemComm

COMMUNICATION

View Article Online
View Journal | View Issue

Cite this: *Chem. Commun.*, 2021, **57**, 3905

Received 5th February 2021,
Accepted 15th March 2021

DOI: 10.1039/d1cc00697e

rsc.li/chemcomm

Hybrid carbon spherogels: carbon encapsulation of nano-titania†

Miralem Salihovic, [a] Jürgen Schoiber, [a] Alexey Cherevan, [b] Christoph Rameshan, [b] Gerhard Fritz-Popovski, [c] Maike Ulbricht, [de] Stefanie Arnold, [de] Volker Presser, [de] Oskar Paris, [c] Maurizio Musso, [a] Nicola Hüsing [a] and Michael S. Elsaesser *[a]

Extraordinarily homogeneous, freestanding titania-loaded carbon spherogels can be obtained using $Ti(acac)_2(OiPr)_2$ in the polystyrene sphere templated resorcinol-formaldehyde gelation. Thereby, a distinct, crystalline titania layer is achieved inside every hollow sphere building unit. These hybrid carbon spherogels allow capitalizing on carbon's electrical conductivity and the lithium-ion intercalation capacity of titania.

Hybrid carbon nanomaterials play a crucial role in various high-performance applications such as energy storage devices (supercapacitors, batteries), photocatalysis, heterogeneous catalysis, or absorption. There are multiple strategies to obtain such hybrids, including bottom-up (sol–gel) and top-down (atomic layer deposition) approaches.[1,2] When implementing metal oxides onto/into carbon structures, it is vital to choose the most suitable carbon substrate carefully[3] and to design the pore structure.[4] The carbon selection must be based on accessibility, electrical conductivity path length, and chemical compatibility.[5] Hollow carbon spheres are a very attractive scaffold for encapsulation and offer a high surface area, high homogeneity, and electrical conductivity. The hollow carbon spheres' void inner space can serve as a storage reservoir, chemical reactor, or drug delivery host.[6–8] The microporous carbon shell acts as a permeable membrane and allows species to diffuse through and fill or drain the interior or initiate a chemical reaction. This nanoreactor concept was recently demonstrated to grow carbon helixes on copper, placed in a carbon hollow sphere material.[9]

Strategies to build-up functionalized hollow carbon sphere materials can be differentiated between post-synthesis or *in situ* approaches. A typical thermal build-up process is the impregnation of hollow carbon spheres with a molten compound, for example, sulfur,[10] germanium,[11] or copper.[12] Other examples of processes for the design of hybrid carbon hollow sphere materials include the ship-in-bottle principle,[13] selective etching,[14] spray pyrolysis, pyrolysis of metal–organic framework (MOF) materials,[15] or layer-by-layer assembly.[16] Such hybrid carbon materials, for example, monolithic titania-loaded carbons, have shown promising results regarding their potential in lithium-ion batteries.[17]

This study presents a versatile template-assisted sol–gel route based on resorcinol-formaldehyde to form monolithic, titania-loaded hybrid carbon spherogels with exceptionally high morphological control. The material properties such as the carbon shell's pore structure or titania/carbon mass ratio can be deliberately adjusted by thermal treatment in CO_2. Our method is a general approach that holds the potential of synthesizing an array of different hybrid carbon spherogels loaded with a variety of metal oxides by choosing adequate metal precursors. Based on our previously described method to carbon spherogels,[18] $Ti(acac)_2(OiPr)_2$ as a titanium precursor is added to the resorcinol-based sol solution. A scheme of the sol–gel process is provided in Fig. 1. Monodispersed, approximately 250 nm-sized (Fig. S1, ESI,† prepared by emulsion polymerization of styrene)[19] polystyrene spheres (3 mass%) in aqueous solution serve as templates for the subsequent resorcinol-formaldehyde gelation process. First, titanium (IV) resorcinol species are formed and arrange around the negatively charged outer surface of the polystyrene spheres (as confirmed by the negative Zeta potential of −20 mV). Thereby, a homogeneous distribution of the Ti(IV) precursor is achieved. During gelation at 80 °C, resorcinol condensation with formaldehyde coats each Ti-layer and interconnects the spheres to form a 3D gel network. After supercritical drying with carbon dioxide, we can reduce linear shrinkage effects to less than 20%. Template removal, carbonization, and titania formation coincide during thermal treatment at 800 °C in argon.

Exemplary, the inset in Fig. 2A shows a photograph of the freestanding, cylindrical, and black-colored hybrid, titania-loaded carbon spherogel (CS–TiO_2/C 800). Thermogravimetric analysis

[a] *Chemistry and Physics of Materials, University of Salzburg, Salzburg 5020, Austria. E-mail: michael.elsaesser@sbg.ac.at*
[b] *Institute of Materials Chemistry, TU Wien, 1060, Austria*
[c] *Institute of Physics, Montanuniversitaet Leoben, Leoben 8700, Austria*
[d] *INM – Leibniz Institute for New Materials, Saarbrücken 66123, Germany*
[e] *Saarland University, Saarbrücken 66123, Germany*

† Electronic supplementary information (ESI) available: DLS and SEM analysis of PS colloids, TGA examination of the ceramic residual content, HAADF image, and EDX scan (STEM) of hybrid hollow carbon spheres, XRD scans of *in situ* crystallization, XPS analysis of titania loading, SAXS scans, nitrogen sorption isotherms. See DOI: 10.1039/d1cc00697e

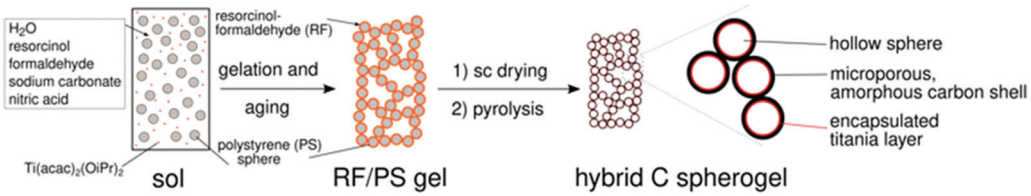

Fig. 1 Schematic representation of the synthesis of hybrid carbon spherogels composed of hollow titania/carbon spheres starting from polystyrene colloids as templates, resorcinol, and formaldehyde as carbon sources titanium diisopropoxide bis(acetylacetonate) as titania source (sc = supercritical drying).

Table 1 Physical and geometric properties of titania loaded carbon spherogels obtained from nitrogen sorption, TEM micrographs, TGA measurements, and SAXS data

Sample	PS template content (mass%)	SSA (QSDFT) (m^2 g^{-1})	Titania content (mass%)	Sphere wall thickness (TEM) (nm)	Sphere interior diameter (TEM) (nm)	Titnia particle size (SAXS) (nm)
CS–TiO_2/C 600	3	713	22	30	220	2
CS–TiO_2/C 1100	3	791	23	30	220	7
CS–TiO_2/C 30 min	3	900	35	22	200	7–15

revealed a complete polystyrene template removal at 470 °C and a ceramic yield (titania) of 22 mass% (Fig. S2 ESI,† and Table 1). For the low resorcinol-to-water molar ratio of 0.008, SEM (Fig. 2A) verifies that the low-density (as measured to be 0.09 g cm^{-3}), macropore-containing spherogel sample is solely composed of hollow spheres. TEM images (Fig. 2B and C) confirm the highly homogeneous structure where each hollow sphere subunit is composed of a distinct titania layer of a thickness of approximately 7 nm (dark grey circle due to pronounced elemental contrast) encapsulated by carbon. This is also supported by energy-dispersive X-ray spectroscopy (EDX) *via* scanning transmission electron microscopy (STEM), which confirms a carbon shell and a titania decoration of the inside wall of the sphere (Fig. 2D and E). This as-prepared titania-loaded carbon spherogel sample (CS–TiO_2/C 800) was amorphous (Fig. 3A) with an average domain size of *ca.* 3 nm (as estimated from a STEM high angle annular dark field image; Fig. S3, ESI†).

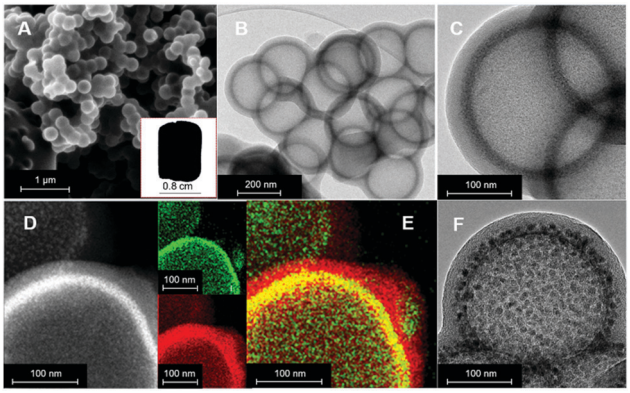

Fig. 2 (A) Scanning electron micrograph (SEM) with a photograph of the freestanding, cylindrical sample (inlet) and (B and C) corresponding transmission electron micrographs (TEM) of hybrid titania carbon spherogels after carbonization at 800 °C (CS–TiO_2/C 800). (D) Elemental analysis by STEM-EDX for elements Ti and C and (E) overlay of both. The corresponding hollow sphere morphology after heat treatment at 1100 °C (CS–TiO_2/C 1100) is depicted in (F).

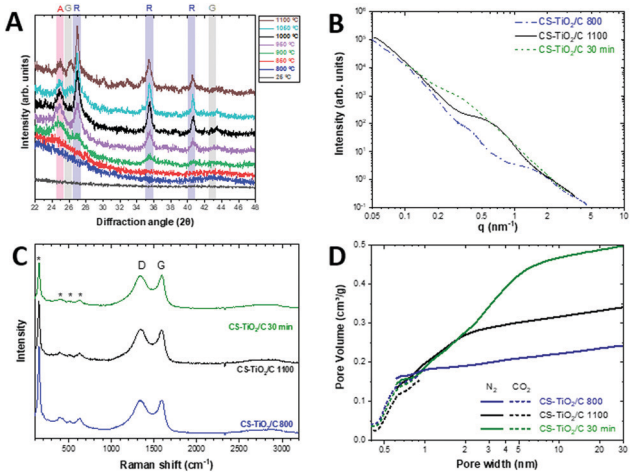

Fig. 3 (A) X-ray diffraction patterns from *in situ* heating of a titania-loaded carbon spherogel from 800 °C to 1100 °C under Ar atmosphere. (B) Small-angle X-ray scattering curves of hybrid titania/carbon spherogel sample as prepared after carbonization (black) and after additional thermal treatment up to 1100 °C (blue). (C) Raman spectra of titania loaded carbon spherogels with the positions of D- and G-mode and titania (marked with asterisks). (D) Differential pore size distributions for titania loaded carbon spherogels from CO_2 and nitrogen sorption (determination for nitrogen using quenched-solid density functional theory assuming slit pore geometry and carbon dioxide using non-local density functional theory).

To confirm the nature of the inner titania coating, X-ray photoelectron spectroscopy was performed after heating in an argon atmosphere (Fig. S4, ESI†). For the pristine carbon spherogel, a C1s signal at 284.4 eV could be observed, with minor impurities from oxygen traces (O1s signal at 532.7 eV) and the corresponding C1s signal at 286.4 eV. With titania loading, a Ti2p signal at 458.9 eV could be observed, corresponding to TiO_2. In the C1s and the O1s signal, new species at 286.9 eV and 534.1 eV align with a TiO_2 layer formation. The O1s signal can be assigned to TiO_2, and the C1s signal results from the TiO_2/carbon spherogel interphase.

The titania crystallite size can be modified by thermal heating as confirmed by *in situ* X-ray diffractometry with temperature steps of 50 °C between 800 °C and 1100 °C under Ar (Fig. 3A). The crystal growth onsets at 900 °C. Samples annealed at 1100 °C are composed of 13 mass% anatase and 87 mass% rutile, as shown by Rietveld analysis. The change in the crystalline size of titania by thermal treatment is also confirmed by TEM (Fig. 2D–F). While the sample at 800 °C displays a homogeneous titania shell (Fig. 2D), the latter breaks up into individual grains (*ca.* 10 nm) confined within the carbon sphere after treatment at 1100 °C (Fig. 2F). Instead of annealing in an inert gas atmosphere, we can further modify the titania-to-carbon ratio by carbon dioxide etching. For example, annealing at a temperature of 800 °C in the presence of carbon dioxide for 30 min results in etching of carbon concomitantly with increasing titania content to 35 mass%, and individual titania grain growth. This CO_2 treatment concurrently consumes carbon *via* oxidation and modifies the titania crystals.

These findings were confirmed by small-angle X-ray scattering (SAXS), showing a power law decay with exponent −2 at low angles, consistent with locally flat structures (Fig. 3B). A pronounced shoulder at larger angles is observed, which shifts to smaller angles upon annealing. This aligns with approximately 2 nm-sized structures, which grow to about 7 nm during annealing at 1100 °C. Thermal activation in CO_2 leads to structures of 15 nm diameter within the shell (Fig. S6, ESI†). The Raman spectra for all titania encapsulated samples (as-synthesized, annealed to 1100 °C and 30 min carbon dioxide etched) show disordered carbon as seen from a D-mode at ∼1345 cm^{-1} and a G-mode at ∼1584 cm^{-1} (Fig. 3C). The presence of titania is confirmed by the presence of four distinct Raman modes in the range of 150–650 cm^{-1}.[20–22]

Nitrogen gas sorption isotherms were recorded at −196 °C (Fig. S7, ESI†) and demonstrate the thermal treatment effect on porosity. The titania-loaded carbon spherogel carbonized at a maximum temperature of 800 °C consists of a dense nano-crystalline titania layer surrounded by a microporous carbon shell and macropores between the spheres. This structure corresponds to a typical type IV isotherm, representing a micro/macroporous material.[23] Thus, the sphere interior's access is limited by the titania nanocrystalline layer, and the H4 hysteresis is only weakly pronounced. By contrast, annealing to 1100 °C initiates titania crystal growth and creates pores within the layer, making the interior accessible. In this case, the desorption isotherm shows a distinct H4 hysteresis loop, typical for macropores enclosed by a microporous shell. The sharp drop at p/p_0 at 0.5 reveals the sudden evaporation of nitrogen from the sphere interior, named tensile strength effect (TSE).[24–26]

By activating the sample for 30 min with carbon dioxide, the hysteresis effect can be even increased, while micropore and mesopore content are enlarged. The corresponding pore size distributions obtained by carbon dioxide sorption verify the sphere shells with mainly micropores <1 nm (Fig. 3D). Therefore, we also observe an increase of the calculated (QSDFT) specific surface areas (SSA) from 713 $m^2\ g^{-1}$ for the as-synthesized sample to 900 $m^2\ g^{-1}$ for the sample treated at 800 °C for 30 min in carbon dioxide (Table 1).

We carried out cyclic voltammetry to characterize the titania nanocrystals' electrochemical behavior in the TiO_2-loaded carbon spherogels. The prepared cells were tested in the potential range of 1.0–3.0 V *vs.* Li^+/Li at various scan rates of 0.1–50 mV s^{-1}. The resulting cyclic voltammograms of CS–TiO_2/C 800 and CS–TiO_2/C 30 min for the first and fifth cycle at 0.1 mV s^{-1} are shown in Fig. 4A. There are no pronounced oxidation/reduction peaks seen in the cyclic voltammogram of CS–TiO_2/C 800; instead, we observed a pronouncedly pseudocapacitive response.[27] The 1st and 5th cyclic voltammogram of CS–TiO_2/C 30 min exhibit a pair of reduction/oxidation peaks at 1.7 V and 2.0 V *vs.* Li^+/Li, which can be ascribed to the Li-ion insertion/extraction in an anatase TiO_2 lattice, respectively.[28]

The increased pseudocapacitive contribution between 3.0 V and 2.0 V *vs.* Li^+/Li may align with micropores' presence within the carbon shell; thereby, ion electrosorption may contribute to the total charge storage process. Comparing the 1st and 5th cycles, we see no noticeable change in the insertion/delithiation peak position. Compared to highly crystalline anatase, there is an increased pseudocapacitive current between 3.0 V and

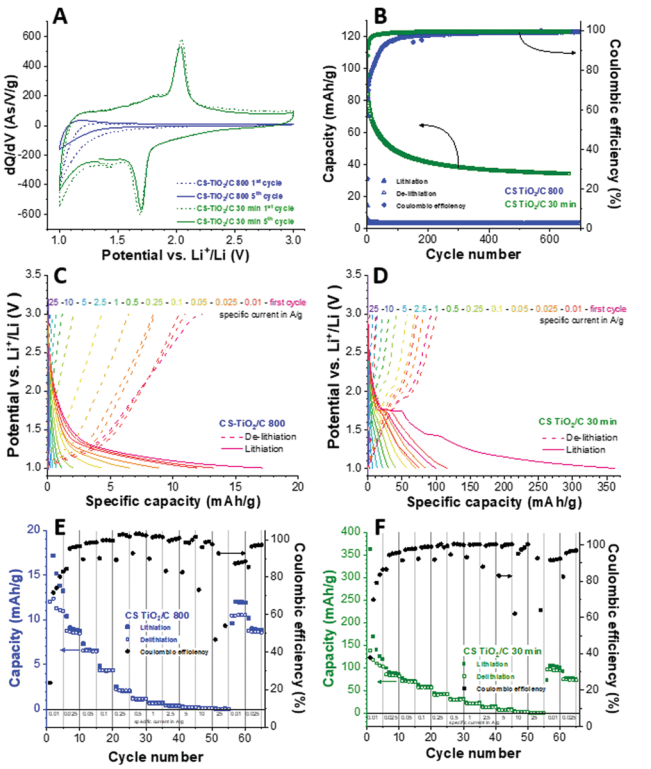

Fig. 4 Electrochemical performance of TiO_2-loaded carbon spherogels. (A) 1st and 5th cyclic voltammogram at a scanning rate of 0.1 mV s^{-1} from 1.0 V up to 3.0 V *vs.* Li^+/Li for CS–TiO_2/C 800 and CS–TiO_2/C 30 min. (B) Galvanostatic charge/discharge cycling performance electrochemical stability with corresponding Coulombic efficiency values at a specific current of 100 mA g^{-1}. (C and D) Galvanostatic charge and discharge profiles at different applied specific currents of 0.01–25 A g^{-1} between 1.0 V and 3.0 V *vs.* Li^+/Li of (C) CS–TiO_2/C 800, and (D) CS–TiO_2/C 30 min. (E and F) Rate performance using galvanostatic charge/discharge cycling with corresponding Coulombic efficiency at different values for the specific current for (E) CS–TiO_2/C 800 and (F) CS–TiO_2/C 30 min.

2.0 V *vs.* Li^+/Li; this contribution becomes particularly evident compared to the current amplitude of the lithiation/delithiation peak. This contribution is most likely aligned with the nanoscopic feature of the anatase domains.

One can further explore the pseudocapacitive feature *via* kinetic analysis, that is, analysis of the rate-dependent current signal. A *b*-value of 0.5 aligns with a diffusion-limited process typical for battery-like processes, while a *b*-value of 1 is expected for an ideal ion electrosorption process.[27] As seen in Fig. S8 ESI,† the pronounced lithiation/delithiation peak of CS–TiO_2/C 30 min shows a *b*-value of 0.6, while the more pseudocapacitive region at 1.25 V *vs.* Li^+/Li has a slightly enhanced *b*-value of 0.62.[29] The capacitor-like response of CS–TiO_2/C 800 aligns with a *b*-value of ~0.8 throughout the potential range of 1.5–3.0 V *vs.* Li^+/Li.

The obtained reduction and oxidation peaks from cyclic voltammetry agree with the galvanostatic discharge and charge profiles in Fig. 4C and D. For the CS–TiO_2/C 800 sample, no plateaus and the associated (redox) reactions can be detected either. In general, a maximum discharge capacity of 12 mA h g^{-1} is obtained at low specific currents. In the CO_2-treated CS–TiO_2/C 30 min sample, we see two plateaus at 1.7 V and 1.4 V *vs.* Li^+/Li during the first lithiation cycle. The first plateau characterizes the Li-intercalation into anatase TiO_2, and the second a reaction of solid electrolyte interphase (SEI) formation. The plateau at 1.7 V disappears in subsequent lithiation curves. A plateau at 2.0 V is observed in the delithiation curves, representing the Li-ion extraction process from Li_xTiO_2.

The rate handing capability of the titania-loaded carbon spherogels was tested with galvanostatic charge/discharge with potential limitation (GCPL) technique applying specific currents between 0.01–25 A g^{-1} at an operational potential of 1.0–3.0 V *vs.* Li^+/Li. The obtained rate handling behavior with the corresponding Coulombic efficiencies are given in Fig. 4E and F. Both tested materials show the expected behavior of proportional decreasing delithiation capacity while applying higher specific current and satisfying capacity retention after returning to the initial current. A significantly higher initial specific delithiation capacity of 137 mA h g^{-1} was obtained from CS-TiO_2/C 30 min with a Coulombic efficiency of 86%. The CS-TiO_2/C 800 sample achieved only a delithiation capacity of 11 mA h g^{-1} with a Coulombic efficiency of 80%. The Coulombic efficiencies of both samples approach ~100% by the 5th cycle and maintained over 98% during the rate capability testing sequence. A specific current of 1 A g^{-1} CS–TiO_2/C 30 min electrodes shows 22 mA h g^{-1} and recovery of *ca.* 100%, while CS–TiO_2/C 800 sample no longer provides any significant charge storage capacity. Fig. 4B shows the cycling stability at 0.1 A g^{-1} of both samples. For CS–TiO_2/C 30 min, there was a loss of 61% capacity after 500 cycles, while CS–TiO_2/C 800 loses nearly all its initial capacity.

For electrochemical application, we see the importance of modifying the CS–TiO_2/C 800 sample further. By reducing the carbon content during the CO_2 heat treatment, it was possible to obtain characteristic electrochemical behavior comparable to that found in the literature.[30–33] The ability to modify the TiO_2/C ratio, TiO_2 properties, carbon porosity, and the apparent option to change from titania to other metal oxides make hybrid carbon spherogels an interesting electrode material for electrochemical applications.

Conflicts of interest

There are no conflicts to declare.

Notes and references

1 S. Fleischmann, A. Tolosa and V. Presser, *Chem. – Eur. J.*, 2018, **24**, 12143–12153.
2 C. J. Shearer, A. Cherevan and D. Eder, *Adv. Mater.*, 2014, **26**, 2295–2318.
3 K. Pfeifer, S. Arnold, Ö. Budak, X. Luo, V. Presser, H. Ehrenberg and S. Dsoke, *J. Mater. Chem. A*, 2020, **8**, 6092–6104.
4 J. Schoiber, C. Koczwara, S. Rumswinkel, L. Whitmore, C. Prehal, F. Putz, M. S. Elsaesser, O. Paris and N. Husing, *ChemPlusChem*, 2021, **86**, 275–283.
5 S. Fleischmann, D. Leistenschneider, V. Lemkova, B. Krüner, M. Zeiger, L. Borchardt and V. Presser, *Chem. Mater.*, 2017, **29**, 8653–8662.
6 S. Li, A. Pasc, V. Fierro and A. Celzard, *J. Mater. Chem. A*, 2016, **4**, 12686–12713.
7 R. J. White, K. Tauer, M. Antonietti and M.-M. Titirici, *J. Am. Chem. Soc.*, 2010, **132**, 17360–17363.
8 W. Meier, *Chem. Soc. Rev.*, 2000, **29**, 295–303.
9 P. M. Gangatharan, M. S. Maubane-Nkadimeng and N. J. Coville, *Sci. Rep.*, 2019, **9**, 10642.
10 T. Yang, Y. Zhong, J. Liang, M. M. Rahman, W. Lei, Y. Chen, M. J. Monteiro, Z. Shao and J. Liu, *Part. Part. Syst. Charact.*, 2017, **34**, 1600281.
11 D. Li, C. Feng, H. Kun Liu and Z. Guo, *J. Mater. Chem. A*, 2015, **3**, 978–981.
12 T. Fu, X. Wang, H. Zheng and Z. Li, *Carbon*, 2017, **115**, 363–374.
13 H. Li, J. Zhao, R. Shi, P. Hao, S. Liu, Z. Li and J. Ren, *Appl. Surf. Sci.*, 2018, **436**, 803–813.
14 X. Li, Y. Xing, J. Xu, Q. Deng and L. H. Shao, *Chem. Commun.*, 2020, **56**, 364–367.
15 H. J. Lee, S. Choi and M. Oh, *Chem. Commun.*, 2014, **50**, 4492–4495.
16 F. Caruso, *Colloid Chemistry II*, Springer, 2003, pp. 145–168.
17 S. Yang, Y. Cai, Y. Cheng, C. Varanasi and J. Liu, *J. Power Sources*, 2012, **218**, 140–147.
18 M. Salihovic, G. A. Zickler, G. Fritz-Popovski, M. Ulbricht, O. Paris, N. Hüsing, V. Presser and M. S. Elsaesser, *Carbon*, 2019, **153**, 189–195.
19 X. Du and J. He, *J. Appl. Polym. Sci.*, 2008, **108**, 1755–1760.
20 O. Frank, M. Zukalova, B. Laskova, J. Kürti, J. Koltai and L. Kavan, *Phys. Chem. Chem. Phys.*, 2012, **14**, 14567–14572.
21 U. Balachandran and N. Eror, *J. Solid State Chem.*, 1982, **42**, 276–282.
22 J. S. Schubert, J. Popovic, G. M. Haselmann, S. P. Nandan, J. Wang, A. Giesriegl, A. S. Cherevan and D. Eder, *J. Mater. Chem. A*, 2019, **7**, 18568–18579.
23 M. Thommes, K. Kaneko, A. V. Neimark, J. P. Olivier, F. Rodriguez-Reinoso, J. Rouquerol and K. S. Sing, *Pure Appl. Chem.*, 2015, **87**, 1051–1069.
24 S. Ikeda, K. Tachi, Y. H. Ng, Y. Ikoma, T. Sakata, H. Mori, T. Harada and M. Matsumura, *Chem. Mater.*, 2007, **19**, 4335–4340.
25 J. C. Groen, L. A. Peffer and J. Pérez-Ramírez, *Microporous Mesoporous Mater.*, 2003, **60**, 1–17.
26 M. Kruk and M. Jaroniec, *Chem. Mater.*, 2001, **13**, 3169–3183.
27 S. Fleischmann, J. B. Mitchell, R. Wang, C. Zhan, D. E. Jiang, V. Presser and V. Augustyn, *Chem. Rev.*, 2020, **120**, 6738–6782.
28 R. van de Krol, A. Goossens and E. A. Meulenkamp, *J. Electrochem. Soc.*, 1999, **146**, 3150–3154.
29 H. Lindström, S. Södergren, A. Solbrand, H. Rensmo, J. Hjelm, A. Hagfeldt and S.-E. Lindquist, *J. Phys. Chem. B*, 1997, **101**, 7717–7722.
30 J. Qiu, P. Zhang, M. Ling, S. Li, P. Liu, H. Zhao and S. Zhang, *ACS Appl. Mater. Interfaces*, 2012, **4**, 3636–3642.
31 X. Xin, X. Zhou, J. Wu, X. Yao and Z. Liu, *ACS Nano*, 2012, **6**, 11035–11043.
32 Y. Ren, Z. Liu, F. Pourpoint, A. R. Armstrong, C. P. Grey and P. G. Bruce, *Angew. Chem., Int. Ed.*, 2012, **51**, 2164–2167.
33 H. Ren, R. Yu, J. Wang, Q. Jin, M. Yang, D. Mao, D. Kisailus, H. Zhao and D. Wang, *Nano Lett.*, 2014, **14**, 6679–6684.

